Numerical Simulations of Collisional Dynamics of Planetary Rings

Heikki Salo

Division of Astronomy, University of Oulu, FIN-90410 Oulu, Finland

Abstract. Numerical simulations of planetary ring dynamics are reviewed, with main emphasis on local 3-dimensional simulations, which utilize a co-moving calculation cell with periodic boundary conditions. Various factors affecting the local balance between collisional dissipation and viscous gain of energy from the systematic velocity field are considered, including gravitational encounters and collective gravitational forces besides physical impacts. Simulation examples of the effects of particle size distribution, particles' spin motion, and different forms of the coefficient of restitution are given. Viscous stability properties are also briefly discussed: examples of both instabilities and overstabilities are given. In this context 2D-simulations are useful, eventhough physically unrealistic even for extremely flattened planetary ring systems.

1 Introduction

Planetary rings consist of numerous small (cm to meter-sized) icy particles orbiting the central planet on nearly circular, almost co-planar orbits. In dense rings the impacts between particles are very frequent, each particle colliding several times per orbital revolution. Even if the impact velocities are small, below 1 cm/s, a significant fraction of random kinetic energy is lost in each collision. An important ingredient in planetary ring dynamics, as compared to many other examples of granular matter, is the presence of a volume force: mean orbital speed depends on the planetocentric distance. This systematic velocity shear provides an energy source which balances the collisional dissipation, leading to a local steady-state in short time scales, in few tens of orbital periods. The steady-state properties, e.g. ring thickness, depend on the amount of dissipation. On the other hand, time scales of radial evolution are much longer, due to low viscosity related to strongly flattened rings.

In what follows I concentrate on dense rings and study their intrinsic evolution with N-body simulations, with parameter values corresponding to Saturn's rings. Technical aspects of the simulations are also summarized. Section 2 provides a brief sketch of basic collisional dynamics relevant to the numerical experiments; for excellent theoretical reviews on ring dynamics, see [30] and [9], the latter dealing also with the influence of external satellites. Local simulations (Section 3) utilizing various laboratory measurements of the elasticity of ice ([3], [10]) yield a wide choice of possible models, ranging from a near monolayer ring to many particle thick multilayers. All these models, corresponding to different surface properties of particles, are in principle allowed by the upper limit for the local ring thickness (about 150 meters), derived from Voyager observations. However, they imply very different viscous stability properties: simulation examples of both viscous instability and overstability are provided in Section 5. The role of self-gravity (Section 4) depends also crucially on the elastic properties, via ring thickness: near monolayer models are susceptible to local gravitational instabilities, which manifest as small scale particle chains. As mentioned in the Summary, there is indirect observational evidence for such local inhomogeneities: this may offer a tool for constraining the actual elastic properties of ring particles.

2 Collisional dynamics of dense rings

The fundamental quantity for collisional rings is the dynamical optical thickness τ, defined as the ratio of the total surface area of particles to the area of the ring they reside in. In dense rings τ is of the order of unity or larger. The importance of optical thickness stems from the fact that for a given size distribution and physical properties of particles, all local dynamical quantities of interest (impact frequency, kinetic temperature, vertical thickness, viscosity etc.) are functions of τ only.

2.1 Impact frequency

The impact frequency between identical particles with radius r can be estimated as $\omega_c \propto n_s \sqrt{T} \sigma$, where n_s stands for the space number density of particles, $\sqrt{T}$ corresponds to 1-dimensional velocity dispersion, and $\sigma = 4\pi r^2$ is the collisional cross-section. The space density n_s can be approximated as n/H, where H is the geometric thickness of the ring, and $n = \tau/\pi r^2$ is the surface number density. Due to collisional partitioning of energy between horizontal and vertical motions, H is proportional to $\sqrt{T}/\Omega$, where Ω is the orbital angular velocity. The explicit $\sqrt{T}$ and n_s dependency thus cancels out, and ω_c depends only on τ. Analytical treatment (e.g. [11]), taking into account the anisotropic distribution of impact velocities and the Gaussian vertical profile, yields $w_c \approx 3\Omega\tau$, or about 18τ impacts/orbital period, in agreement with simulations. As a typical period in Saturn's rings is about 10 hours, each particle in dense rings collides several times/hour.

2.2 The establishment of local energy equilibrium

The dissipation in mutual impacts tends to decrease particle's orbital eccentricities and inclinations, and thus the kinetic energy stored in random motions. On the other hand, the colliding particles have typically slightly different semi major axis. Since the distribution of impact directions is more or less random, energy is transferred from the systematic velocity field to random motions.

The local kinetic temperature is thus determined by the balance between the viscous gain of energy from the orbital motion ($\dot{E}_{visc}$) and the loss of energy in dissipative impacts ($\dot{E}_{coll}$). The energy gain (per unit mass) is related to kinematic viscosity ν by $\dot{E}_{visc}=\nu(Rd\Omega/dR)^2 = \frac{9}{4}\nu\Omega^2$ in a Keplerian velocity field with $\Omega \propto R^{-1.5}$. The kinematic viscosity is usually divided into two parts [1], to the local viscosity ν_L due to the transport of angular momentum via particles' radial excursions, and to the non-local viscosity ν_{NL} arising from the angular momentum exchange in impacts between finite-sized particles at slightly different radial distance.

The basic expression for local viscosity is $\nu_L = \omega_c l^2$, where l is the radial mean free path. In high impact frequency regime l^2 is proportional to T/ω_c^2 while for $\omega_c/\Omega \to 0$, epicyclic motions set an upper limit $l^2 \approx T/\Omega^2$. A semi-empirical formula consistent with these limits yields (holds within 10% accuracy in simulations with $\omega_c/\pi\Omega < 1$)

$$\nu_L \approx \frac{1.35T\omega_c}{(\pi\Omega)^2} \; \frac{1}{(\omega_c/\pi\Omega)^2+1} \tag{1}$$

The functional form of non-local viscosity is less clear. Analytical estimates ([9]) suggest that $\nu_{NL} \approx \omega_c r^2$, whereas simulations indicate that ν_{NL} also increases slightly with $\sqrt{T}/\Omega r$. In any case, ν_{NL} may become significant compared to ν_L if τ is moderately large and the system is not far from the monolayer state ($\sqrt{T}/r\Omega < 3$).

The energy loss in impacts can be approximated as

$$\dot{E}_{coll} = -1/2\; \omega_c T(1-{e_n}^2), \tag{2}$$

where e_n is the normal coefficient of restitution. An isotropic Gaussian distribution of impact velocities is assumed, and the loss due to friction is assumed to be negligible.

Two basic types of equilibrium behaviour can be expected, related to whether ν_L or ν_{NL} gives the dominant contribution to the energy gain. If $\nu_L >> \nu_{NL}$ (hot system with $\sqrt{T} >> r\Omega$) the equilibrium condition $\dot{E}_{visc} + \dot{E}_{coll} = 0$ implies

$$(1-{e_n}^2) = \frac{0.6}{(\omega_c/\pi\Omega)^2+1} \tag{3}$$

As ω_c depends only on τ, the equilibrium requires a specific value $e_n = e_{cr}$ for each τ. This equation is practically identical to the well-known Goldreich-Tremaine [8] formula $(1-{e_n}^2)(1+\tau^2) = 0.61$, derived from their semi-numerical solution of the collision integral. It also agrees with the treatment by Hämeen-Anttila ([11]; see also [30]) where the collision integral is solved by an analytical approximation. On the other hand, in a cool system $\nu_{NL} \simeq \nu_L$, and the additional energy input due ν_{NL} requires larger dissipation and thus lowers the implied e_{cr}; in this case the value of steady-state e_n depends also on the ratio $\sqrt{T}/r\Omega$, and can be quite different from that of Eq. (3). The two different theoretical $e_{cr}(\tau)$ relations are shown in Fig. 1.

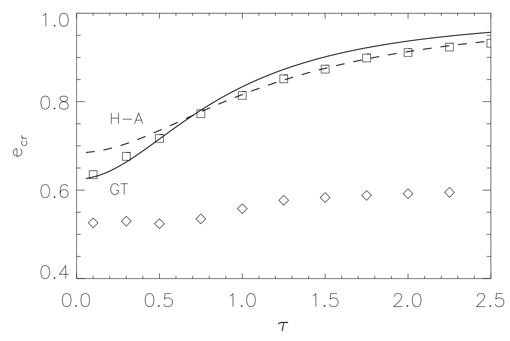

Fig. 1. Theoretical e_{cr} vs. τ dependency, according to [8] (GT), and [11] (H-A). Also shown are the effective values of e_n in two series of simulations: the upper points correspond to a 'hot' system (velocity dependent elasticity according to Model IV in Fig. 2), while the lower points correspond to a near monolayer (Model I with 1 meter particles). The effective e_n in simulations is measured by $\overline{e_n v_n^2}/\overline{v_n^2}$

Laboratory measurements of ice ([3], [10]) as well as theoretical work ([6], [29], [4]) indicate that e_n is a decreasing function of the perpendicular component (v_n) of impact velocity (Fig. 2). In this case T adjusts to a steady-state, where the effective value of e_n depends on τ via the energy balance equation. This steady-state is stable if $de_n/dv_n < 0$, as also implied by measurements: for example, if the instantaneous T exceeds the steady-state value, $|\dot{E}_{coll}| > E_{visc}$ and the system cools toward the steady state.

The average v_n and thus also T corresponding to $e_{cr}(\tau)$ depend on the functional form of $e_n(v_n)$. According to laboratory measurements, elasticity is very sensitive to the surface properties of particles; it may also depend on the particle size via the curvature of the impact point. As the actual properties of particles in planetary rings are not known, these measurements leave a wide margin for possible local steady-state properties. Especially, the most widely adopted elasticity model, that of Bridges et al. [3], with $e_n = 0.32{v_n}^{-0.24}$ (v_n expressed in cm/s) implies a near monolayer ring. Simulation examples with this (Model I) and the other models of Fig. 2 will be provided in Section 4.

What happens if e_n is constant, independent of impact velocity? In this case the critical value e_{cr} defined by Eq. (3) divides between stable and unstable temperature behaviour: if $e_n > e_{cr}(\tau)$, then $|\dot{E}_{coll}| < E_{visc}$ and T increases with time, leading to dispersal of the system. On the other hand, for $e_n < e_{cr}(\tau)$ the energy gain due to ν_L is less than required by dissipation, and T decreases. However, eventually the contribution by ν_{NL} balances the dissipation. The minimum value of $\sqrt{T}$ depends on the value of the constant

e_n, but is typically few times $r\Omega$. Note that even in the case of $e_n(v_n)$ the behaviour can be quite similar to that of a constant $e_n < e_{cr}$, provided that $e_n(v_n)$ drops below e_{cr} already for $v_n \sim r\Omega$. Especially, Bridges et al. model behaves in this way if applied to meter-sized particles in Saturn's rings, yielding a practically indistinguishable steady-state as compared to $e_n \approx 0.5$ (see below, Fig. 4), due to the dominant role of ν_{NL} in both cases.

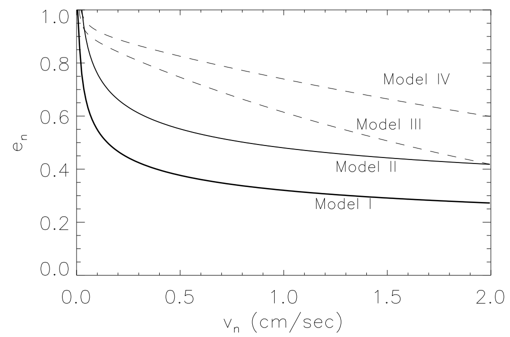

Fig. 2. Elasticity models. Solid lines denote fits to laboratory measurements with frosty ice particles, in two different temperatures ([3], Model I; [10], Model II). Dashed lines correspond to measurements in [10], with particle sizes r=2.5 and 20 cm (Models III and IV, respectively), where particles have compacted frost on their surfaces

2.3 Radial Evolution

The conservation of total angular momentum, combined with the dissipative loss of total energy, implies that a ring system as a whole must spread with time (however, this does imply that *local* density variations will necessarily smooth out, see Section 5). The characteristic spreading time for a ring region with radial width W is $T_{spread} \simeq W^2/\nu$. Assuming $\sqrt{T} = kr\Omega$ and $\nu \approx T/\Omega$ (as for τ of the order of unity), $T_{spread} \approx 10/k^2(W/r)^2$ orbital periods. For example, for a region with $W \approx 10^3$ particle radii (about 1 km), $T_{spread} \approx 10^5$ orbital periods if the ring is near a monolayer state ($k \approx 3$). This is already very long compared to the time-scale of the establishment of local energy balance. For the whole of Saturn's rings, spreading times for the near monolayer models are of the order of the age of the Solar System [2].

3 Simulations of collisional rings

The local collisional dynamics of planetary rings is theoretically fairly well understood, and the steady-state properties can be estimated analytically from the kinetic theory ([8], [11], [1], [21]), even if size distribution and gravitational encounters are included [13]. Numerical simulations are still necessary for many reasons. Especially, they allow the accurate treatment of dense, flattened rings where finite-size effects become important. Also, the realistic inclusion of collective self-gravity (see Section 4), is still out of scope of analytical treatments.

3.1 Early simulation studies

The pioneering simulation studies of the collisional evolution of planetary rings were performed by Trulsen ([34]), Brahic ([2]), and Hämeen-Anttila & Lukkari ([12]). All these simulations used the same approach: a complete ring of particles orbiting the central body in Keplerian orbits. Since only few hundred particles could be followed, these simulations were limited to low τ. Also, the particle sizes were large as compared to the width of the ring, which made it difficult to separate local evolution from the radial spreading.

Nevertheless, many basic characteristics of collisional systems were revealed, including the existence of the critical value for the coefficient of restitution [34], the minimum residual velocity dispersion of the order of $r\Omega$ [2], and the establishment of equilibrium with finite velocity dispersion for $e_n(v_n)$ [12]. These simulations also served as important checks for various analytical treatments (see [30]).

3.2 Local simulations

Local simulations offer a possibility to simulate dense rings, by restricting calculations to a small co-moving region orbiting inside the rings (Fig. 3). Due to systematic velocity shear individual particles tend to leave the calculation region, which is taken into account by periodic boundary conditions. The main advantage of the method is that radial spreading is prevented, thus facilitating the study of local steady-state properties as a function of fixed τ. This is justified, based on the large separation of local and radial time scales. Local method was first applied to planetary ring simulations by Wisdom and Tremaine ([37]) and to stellar disks by Toomre ([33]). In the former study impacts between identical particles were taken into account, but not their mutual gravity, whereas the latter study treated only gravitational forces.

Local Method As the typical size of the calculation region is very small compared to the radial distance from the central body, linearized equations of motion can be used

$$\begin{aligned} \ddot{x} - 2\Omega\dot{y} + (\kappa^2 - 4\Omega^2)x &= F_x \,, \\ \ddot{y} + 2\Omega\dot{x} &= F_y \,, \\ \ddot{z} + {\Omega_z}^2 z &= F_z \,. \end{aligned} \tag{4}$$

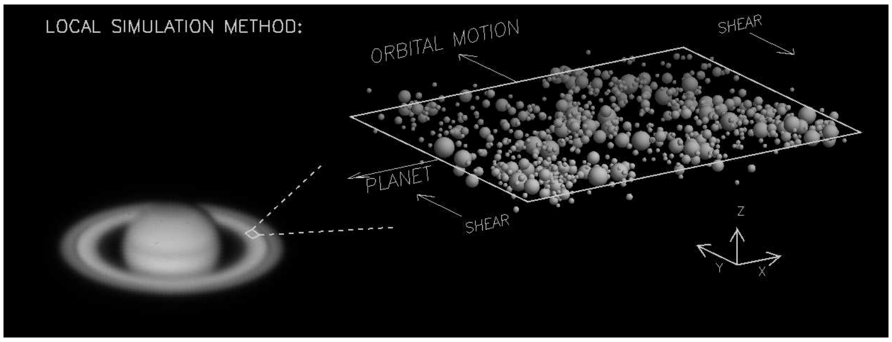

Fig. 3. Schematic representation of local simulation method

Here the x-axis points in the radial direction, the y-axis in the direction of orbital motion, and the z-axis is perpendicular to the equatorial plane. The reference point of the coordinate system moves with angular velocity of Ω in a circular orbit at a radial distance a. In the case of a central point mass, the epicyclic frequency κ and the frequency Ω_z of vertical oscillations are both identical to Ω. F_x, F_y, F_z denote additional forces, e.g. self-gravity.

The boundaries are treated by assuming that each particle with a position (x, y, z) has an infinite set of image particles at $(x + nL_x, y + mL_y - 3/2nL_x\Omega t, z)$, where m and n are integers, L_x and L_y denote the dimensions of the actual calculation region, and t the time reckoned from the beginning of the simulation. Eqs. (4) are invariant under this transformation. Each time a particle crosses the boundary, one of its images enters the box. If the crossing occurs across the inner or outer boundary, the velocity of the particle is modified by $\Delta\dot{y} = \pm 3/2\ \Omega L_x$, which corresponds to the difference of shear velocity across L_x. In this manner the evolution of the system is independent of the choice of the origin of the coordinate system. The results are also independent of the size of the calculation region, provided that it is large compared to the mean free path between impacts ([37],[23]).

Treatment of impacts In most local simulations ([37],[23], [24], [25] , [20]) the standard impact model with instantaneous velocity changes has been used. Tangential coefficient of restitution, e_t, can also be included, besides e_n, in which case the exchange of energy with particle's spin motion must also be taken into account. The velocity change in impact is determined by [21]

$$(\boldsymbol{v}_1)_{coll} = -e_n \boldsymbol{c}\boldsymbol{c} \cdot \boldsymbol{v}_{coll} + e_t \boldsymbol{c} \times (\boldsymbol{v}_{coll} \times \boldsymbol{c}), \tag{5}$$

where $(\boldsymbol{v}_1)_{coll}$ and $(\boldsymbol{v})_{coll}$ stand for the post- and pre-collisional velocity differences at the contact point and $\boldsymbol{c}$ for the unit vector joining the particle centers. In terms of $\boldsymbol{v} = \dot{\boldsymbol{R}}' - \dot{\boldsymbol{R}}$, the relative velocity of particle centers, $(\boldsymbol{v})_{coll} = \boldsymbol{v} - (r\boldsymbol{\omega} + r'\boldsymbol{\omega}') \times \boldsymbol{c} + (r + r')\Omega \boldsymbol{N} \times \boldsymbol{c}$, where r and $\boldsymbol{\omega}$ denote the particle radius and spin-vector (primed and unprimed symbols distinguish the two particles). The last term, $(r+r')\Omega \boldsymbol{N} \times \boldsymbol{c}$, where $\boldsymbol{N}$ is the unit vector in the direction perpendicular to the equatorial plane, arises due to the rotating coordinate system. The changes of the velocity and spin vector of an individual particle follow from the conservation of linear and angular momentum, yielding (for homogeneous spheres)

$$\dot{\mathbf{R}}_1 - \dot{\mathbf{R}} = \frac{m'}{m+m'}\{(1+e_n)\boldsymbol{cc}\cdot\boldsymbol{v}_{coll} + \frac{2(1-e_t)}{7}(\boldsymbol{v}_{coll} - \boldsymbol{cc}\cdot\boldsymbol{v}_{coll}\}, \tag{6}$$

$$(r\boldsymbol{\omega}_1 - r\boldsymbol{\omega}) = \frac{m'}{m+m'}\frac{5(1-e_t)}{7}\boldsymbol{c}\times\boldsymbol{v}_{coll}, \tag{7}$$

where m and m' are the masses of the impacting bodies. A simple model for slightly non-spherical shape has also been studied, by assuming that the tangent plane of impact is not exactly perpendicular to $\mathbf{c}$, but deviates from it by a small random amount in each impact [21].

Search of impact pairs The speed of the collisional simulation depends crucially on the efficient search of impact pairs. For example, [37] uses the fact that orbits between impacts are Keplerian epicycles, and solves iteratively for the intersection time of each pair of epicycles. The impact of the pair with the smallest impact time is executed and their post-impact elements are calculated, leading to updated intersection times with all the other particles. The system is thus moved from one impact to the next ("event-driven" method). This is fairly fast for small particle numbers (≈ 50 in [37]), but as N increases, checking of all $N(N-1)/2$ pairs gets excessively slow.

For larger N it is advantageous to integrate the equations of motions, and during each time-step search for impacts with the help of a second-degree Taylor-polynomial [23]. This also allows inclusion of additional forces. Even then it is importantant to limit the number of pairs examined. This can be done quite efficiently by keeping track of the maximum pre-step separation actually leading to an impact, and by checking in each step only those pairs whose distance does not exceed this maximum multiplied by some threshold value. This threshold must be chosen in a manner which ensures that no impacts are lost, and it also must be dynamically adjusted as the temperature of the system evolves. In practice, the number of pairs examined is proportional to $\sqrt{T}/(r\Omega)N$. Note that the actual integration needs not to be performed by Taylor-series: for example in [24] a fourth order Runge-Kutta integration is utilized, and the impact locations initially estimated by the second-degree expansion are iteratively improved to correspond to the full accuracy of the integration. It must be stressed that it is important to take correctly into account impacts taking place over boundaries. For small calculation regions this fraction can be quite significant, and the omission of such impacts will modify the energy balance.

3.3 Results of Local Simulations

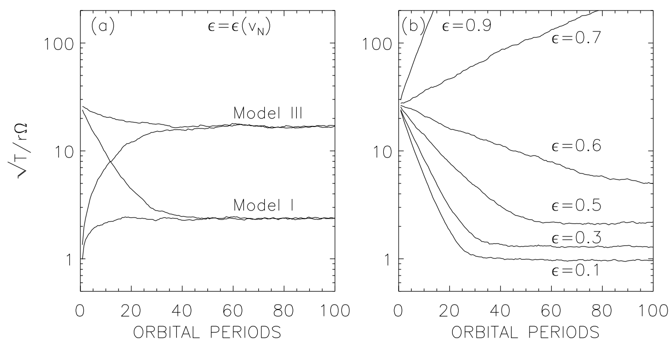

Fig. 4. Examples of time evolution in simulations. Frame (a) compares two $e_n(v_n)$ models of Fig. 2, starting from different initial values. Temperature is calculated by $T = (c_1^2 + c_2^2 + c_3^2)/3$, where c_1, c_2 and c_3 denote the principal axis components of velocity ellipsoid. In each simulation $r = 1$ m, Saturnocentric distance $a = 100\ 000$ km, and $\tau = 0.1$. In (b), evolution with different constant values of e_n is studied: for $\tau = 0.1$, $e_{cr} \approx 0.65$. $e_t = 1$ is assumed in these and all subsequent simulations, unless otherwise indicated

Simulations of identical particles Fig. 4 displays typical examples of time evolution in collisional simulations. Regardless of the initial values, the system establishes a steady-state where T and other dynamical quantities stay on a constant level. The timescale to reach steady-state is typically of the order of 50-100 impacts/particle. The only exception is a case with constant $e_n > e_{cr}$ for which no steady-state exists. In the case of constant $e_n < e_{cr}$ the steady-state $\sqrt{T}$ is proportional to $r\Omega$. For $e_n(v_n)$ the steady-state depends drastically on the parameters of the elasticity model, as anticipated in Section 2. Once the steady-state is obtained, various dynamical quantities can be collected very accurately by averaging over long time spans. Especially, both local and non-local viscosity can be determined from the flow of angular momentum, averaged over all particle orbits and impacts, respectively [37].

In Fig. 5 some interesting dynamical properties are plotted as a function of τ. The main effect of increased density is the reduction of $\sqrt{T}$, basically because E_{visc} becomes less effective as the mean free path between impacts is reduced. In Fig. 5 this is studied in terms of the geometric thickness H, which is roughly proportional to $\sqrt{T}$ (except in flat systems with large τ, where the piling of particles thickens the system although T is almost constant). The elastic models of Fig. 2 lead to even a factor of 10 difference in H. This difference also reflects in the local and, to a lesser degree, in the non-local contribution to ν. For a cool system the product $\tau\nu$ is monotonically increasing, because of the dominant role of ν_{NL}, whereas for a hot system it may have a decreasing portion at large τ regime, due to the reduction of ν_L. As discussed in Section 5, negative $d(\tau\nu)/d\tau$ leads to radial instability, whereas strong enough positive slope may indicate overstability.

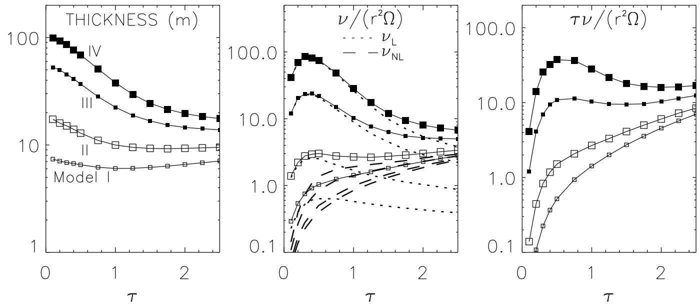

Fig. 5. Dependency of geometric thickness and viscosity on τ, for the various elastic models. Geometric thickness is defined by $H^2 = 12\overline{z^2}$. As in Fig. 4, $r = 1$ m and $a = 100\ 000$ km

Simulations with size distribution According to Voyager measurements, the size distribution of particles in Saturn's ring can be approximated with a power-law [18]

$$dN/dr \propto r^{-q}, \quad 1 \text{ cm} < r < 5 \text{ m} \tag{8}$$

with $q \approx 3$. Size distribution leads to a steady-state where kinetic temperature of small particles exceeds that of the large ones (Fig. 6). However, the system is still far from equipartition of energy: depending on the elastic model, the kinetic energy of smallest particles is about 2-20% of that of the largest ones. In simulations, due to limited N the width of the distribution is smaller than in reality. Simulation tests [24] indicate that the effect of this truncation is small as long as $r_{max}/r_{min} > 10$, and correct r_{max} is used. In the case of constant $e_n < e_{cr}$, or with the Bridges-model, the thickness of the layer of the largest particles is proportional to r_{max}. The same scaling holds for the whole distribution as the behaviour of small particles is governed mainly by the dynamical state of the largest ones. The viscosities experienced by the small particles exceed those for the large ones, but otherwise the $\nu(\tau)$ behaviour is similar to that in the case of identical particles. Especially, simulations show no signs of selective viscous instability among small particles, which in principle could be possible if the system were closer to equipartition of energy (see [30]).

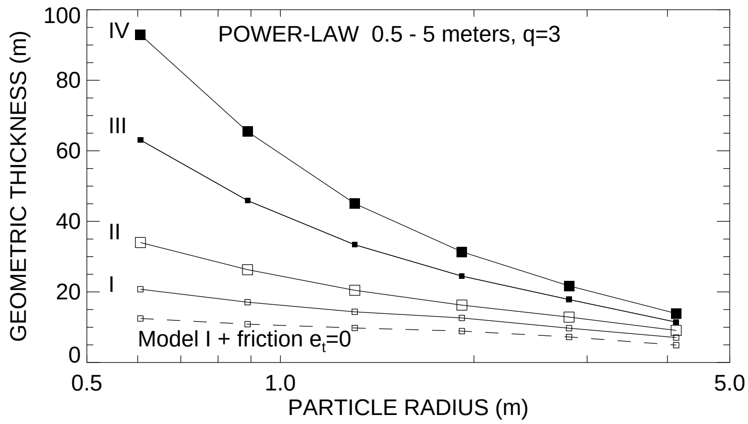

Fig. 6. Geometric thickness H in simulations with size distribution, for $\tau = 1.0$. Particles are divided to six logarithmic size-groups. Also indicated is the maximal effect of tangential friction, in combination with the Bridges-model (Model I).

Fig. 6 illustrates also the effects of friction, with $e_t = 0$. This represents the maximal amount of extra dissipation due to friction, and is able to reduce H to about one half. However, measurements indicate that in reality e_t is close to unity [31]. Friction also leads to partitioning of energy between random motions and spin degrees of freedom: in general, for identical particles $E_{spin}/E_{random} \approx 2(1-e_t)/(9+5e_t)$ [21]. In the case of size distribution, small particles obtain relatively larger share of spin-energy, but the above ratio holds for the distribution as a whole. Spin-axes also acquire a residual mean orientation, $\overline{\omega_z} \approx 0.3\Omega$, indicating rotation in the same sense as the orbital motion. However, for the smallest cm-sized particles this mean is insignificant compared to the dispersion of ω_z (roughly $\propto 1/r$), so that their spin-axis are practically randomly oriented.

4 Self-gravity

4.1 Expectations

The inclusion of particles' mutual gravitational forces affects the local dynamics of collisional systems on several, partially competing ways. For low τ the main effect comes from close binary encounters, which correspond to totally elastic impacts: the kinetic energy of the encountering pair is conserved, while the deflection of orbits transfers energy from the systematic to random motions. This extra heating will tend to increase $\sqrt{T}$, until it becomes comparable to the escape velocity from particle surfaces [5]. This corresponds to minimum $H \approx 10$ meters for the parameter values of Fig. 5 (assuming solid icy density, $\rho = 0.9$ g/cm^3). If collisions alone are able to maintain larger H, the effect of encounters is negligible.

For a system with larger τ, the mean vertical self-gravity can exceed the corresponding component of the central force. For identical particles this takes place if

$$H < 4\tau r(\rho/\rho_{plan})(a/r_{plan})^3, \tag{9}$$

where r_{plan} and ρ_{plan} are the radius and internal density of the planet (60 000 km and 0.7 g/cm^3 for Saturn). Inclusion of this extra force tends to reduce H quite markedly, both because of increased frequency of vertical oscillations and via increased impact frequency leading to enhanced dissipation. For the parameters studied in Fig. 5, the above condition is fulfilled for the coolest model when $\tau > 0.3$.

Intuitively, planar components of self-gravity may be expected to have less importance, due to partial cancellation of forces. However, as shown in [32], a differentially rotating disk is locally unstable against the growth of axisymmetric disturbances, if its radial velocity dispersion falls below the critical value $c_{cr} = 3.36G\Sigma/\kappa$. The first radial wavelength to become unstable corresponds to $\lambda_{cr} = 4\pi^2 G\Sigma/\kappa^2$. Even for Toomre parameter $Q_T = c_{rad}/c_{cr} \approx 2-3$, such system is susceptible to the growth of local, non-axisymmetric disturbances ([14]). In Keplerian potential this gravitational instability manifests as trailing density enhancements, forming about 25^o angle with respect to tangential direction. In the case of stellar systems, the heating accompanying these disturbances eventually suppresses them: in the case of particulate rings collisional dissipation can lead to a statistical steady-state, where new structures continuously emerge and dissolve. The condition $Q_T < 2-3$ is comparable to Eq. 9, indicating that whenever the vertical field is important, the system is also susceptible to collective horizontal instabilities.

4.2 Simulations of self-gravitating systems

The first simulations of self-gravity, performed with azimuthally complete systems, included only gravitational encounters ([17]). They illustrated the extra heating due encounters but had little significance for dense rings. On the other hand, in [37] the mean vertical self-gravity was included by applying a constant enhancement factor $\Omega_z/\Omega = 3.6$ in the equations of motion, approximating the expected situation in Saturn's B-ring. In these simulations the vertical self-gravity led to a reduced vertical thickness and strong enhancement in the impact frequency, as expected, and when compared to the non-gravitating case, a much larger non-local viscosity was obtained.

When self-gravity is correctly included (see Fig. 7), the collective gravitational instability overshadows the effects of enhanced vertical field and leads to dramatically different behaviour: near monolayer systems develop transient density enhancements, "wakes", each forming and dissolving in timescales of few orbital periods [25]. The scattering of particles by these wakes leads to

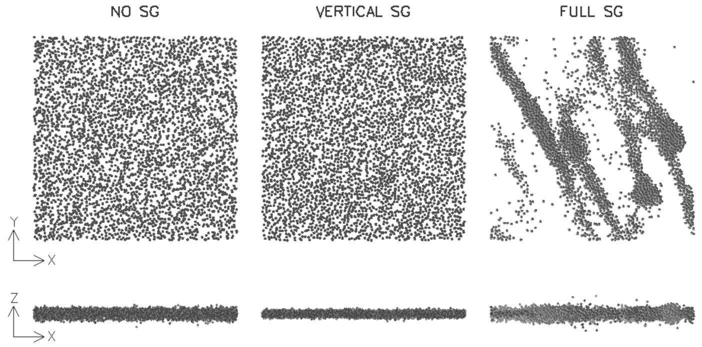

Fig. 7. Comparison of simulations either neglecting self-gravity (left), including just the vertical self-gravity (middle), or all components of self-gravity (right). In each case $a = 100\ 000$ km, $r = 1$ m, $\tau = 0.75$ and Bridges et al. elasticity model is used. In the self-gravitating cases $\rho = 0.9$ g/cm^3. Size of the square-shaped calculation region is 125 m

enhanced velocity dispersion and thickening of the ring: the steady-state corresponds to $Q_T \approx 2-3$, as anticipated. Spatial autocorrelation analysis shows close correspondence to Julian-Toomre ([14]) stellar wakes.

Simulation of gravitating systems requires quite large calculation regions. The scale of the wakes is proportional to λ_{cr} ($\sim$ 100 meters), and in order to obtain wake amplitudes and directions which are independent of the periodic boundaries, L_x and L_y must exceed about $4\lambda_{cr}$. This implies

$$N \approx 2200\tau^3(\rho/0.9\ \mathrm{gcm}^{-3})^2(a/100\ 100\ \mathrm{km})^6(L_x/\lambda_{cr})(L_y/\lambda_{cr}) \qquad (10)$$

Simulations thus become computationally very demanding for large τ, especially when the outer edge of the rings ($a = 137\ 000$ km) is approached.

Whether or not collective wakes occur, depends crucially on the elasticity. If the collisions alone are able to keep $Q_T \geq 3$, no wakes can form. Applied to Saturn's rings this implies that local inhomogeneities may be expected only for rather dissipative cases, corresponding roughly to Bridges et al. elasticity model. On the other hand, smaller dissipation in impacts, as implied by any of the other three models studied, will suppress wakes.

At large distances gravitational accretion of particles is observed. The condition that the attraction between two contacting, radially aligned, synchronously rotating identical particles exceeds the tidal force due to planet is (see e.g. [35])

$$(a/r_{plan})^3 > 12(\rho_{plan}/\rho), \qquad (11)$$

whereas in the case of two very different sized particles the factor 12 is replaced by 3. For particles with $\rho = 0.9$ g/cm^3 this implies $a = 126\ 000$ and 80 000 km, respectively. However, in actual rings the non-zero velocity dispersion makes accretion more difficult ([19], [25], [26]), and the limiting distances for the formation of aggregates are shifted outward. Fig. 8 illustrates accretion: as a is increased the wakes begin to degrade into particle groups. For identical particles the group formation becomes efficient for $a \approx 140\ 000$ km, whereas in the case of size distribution this occurs already for $a > 125\ 000$ km.

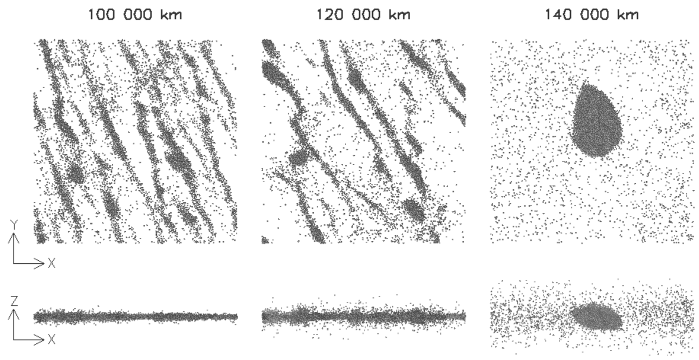

Fig. 8. Effects of self-gravity at different distances

4.3 Numerical methods in self-gravitating simulations

The simulation of self-gravity poses some technical problems, besides the large CPU-time consumption needed for the evaluation of mutual forces. Namely, as mentioned above, beyond a certain planetocentric distance the net force between a pair of particles in contact can become directed toward each other. This means that the method of treating collisions in terms of instantaneous velocity changes becomes insufficient: every now and then some particles will penetrate each other, leading to an artificial increase in the density of wakes and particle groups. If allowed, this would lead to unreliable results concerning particle accretion.

The solution is to include explicitly the pressure forces affecting in the impact. In [26] this is done in terms of the linear visco-elastic model, originally developed in [6] for the theoretical parameterization of measurements of velocity and size-dependent elasticity. The impact force is expressed as

$$F(\alpha) = k_1 \alpha + k_2 \dot{\alpha}, \tag{12}$$

where $\alpha = (r + r') - |\boldsymbol{R} - \boldsymbol{R}'| > 0$ is the penetration depth during the impact. Thus in the gravitational simulations, instead of searching for exact impact times, this extra force is included between colliding, slightly penetrating particles, and the motion is integrated through the impact with small time steps. The CPU-time consumption can be kept tolerable, provided that the impact duration, T_{dur} is not too long. The attractive feature of the above simple force model when applied to simulations is that the constants k_1 and k_2 can be easily tied to the desired T_{dur} and e_n [26]. Also $e_n(v_n)$ can be simulated, if the parameters are chosen according to the pre-impact velocity. The results are identical to those when calculating instantaneous impacts, as long as T_{dur} is less than, say 10^{-3} orbital periods. In principle, more realistic theoretical impact models, like the Hertzian law (see [29]) can be used in simulations, but then the various scalings would become more complicated.

The calculation of gravitational forces is done either with direct summation, or in the case of large N, with a combination of direct summation for the nearby particle pairs and a 3-dimensional grid evaluation for the distant gravity, with FFT utilizing the periodicity in planar coordinates. A tree-method has also been used ([20]), but there is no clear advantage over the grid method. Note that nearby forces must in every case be evaluated accurately, in order to include the gravitational encounters correctly.

5 Radial evolution

The most puzzling features of Saturn's rings, revealed by Voyager fly-bys, are the radial density variations seen on all scales down to the resolution limit of few kilometers. Their origin has inspired a great deal of theoretical efforts, mainly on the role of perturbations due Saturn's inner satellites (see [9]). Indeed, the radial distances of the most regular density oscillations in the outer A-ring agree with locations of satellite resonances. However, resonances are too rare to explain the less regular variations in the densest B-ring. It appears inevitable that irregular density variations must have an intrinsic origin, related to some type of instability in dense collisional rings.

The originally proposed intrinsic mechanism was the viscous instability ([11], [36], [15], [16]), based on the assumption that there is a large collision-induced difference between the kinetic temperatures of rarefied (hot) and dense (cool) portions of the rings. In this case the dynamic viscosity, proportional to $\tau\nu$, may decrease with τ (as in the two 'hot' examples of Fig. 5), leading to collisional particle flux which is directed toward local density maxima. However, even if in principle possible for very elastic particles, the instability should lead to a bimodal density distribution, not consistent with observations.

A more promising possibility is the viscous overstability, which can take place if viscosity increases strongly enough with τ [27]. The linear stability analysis in [27] suggests that the B-ring should be overstable, with most overstable wavelengths of about 100 meters, having e-folding times of only few orbital periods. Superposition of such overstable waves, with amplitudes saturated by non-linear phenomena, might well yield similar structures as seen in the B-ring [28]. According to [27] the condition for overstability is that $\beta = (d\nu/d\tau)(\tau/\nu) > \beta_{cr}$ where β_{cr} is about 0.11. If self-gravity is included (however, assuming only strictly axially symmetric waves), β_{cr} is reduced to even slightly negative values ([27]). The condition for the viscous instability corresponds to $\beta < -1$.

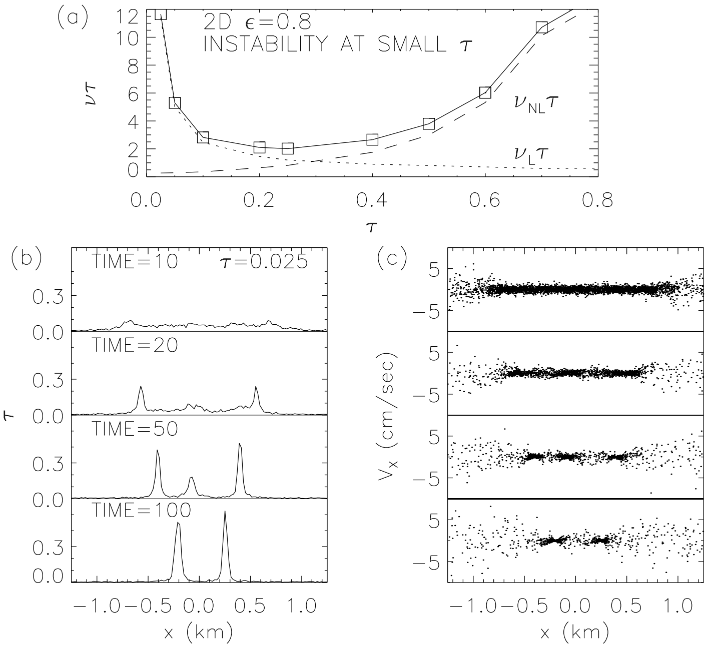

Fig. 9. Instability in 2D simulation with $e_n = 0.8$. Frame (a) shows the dependency of $\nu\tau$ vs. τ from a series of small-N simulations, while frames (b) and (c) display snapshots of radial density distribution and velocity profile in a simulation with radially extended calculation region ($L_x = 4000$ m, $L_y = 125$ m, $N = 4000$), for $\tau = 0.025$. Time is reckoned in orbital periods. Note that while illustrating the instability at small τ, this strictly 2D simulation has no relevance to real rings, even if they were in *near* monolayer state: if vertical motions were allowed, the system would rapidly disperse due to high e_n exceeding the 3D e_{cr}

With local simulations the radial evolution can be studied in two complementary ways. Firstly, it can be addressed by analytical means, e.g. with linear stability analyses similar to that in [27], utilizing viscosity vs. density dependency found in moderately small N simulations conducted for various $\tau's$. Secondly, the radial evolution, say in scales less than few kilometers, can also be studied directly, by a large N simulation with radially extended calculation region. This provides also a check for the results of stability analyses.

Two-dimensional simulations allow easy demonstration of both the above mentioned types of unstable behaviour. The basic difference as compared to 3-dimensional system is that in the 2D case $\omega_c \propto \sqrt{T}\tau$ (for small τ). This follows because the 2D system can not adjust its space density via vertical thickness.

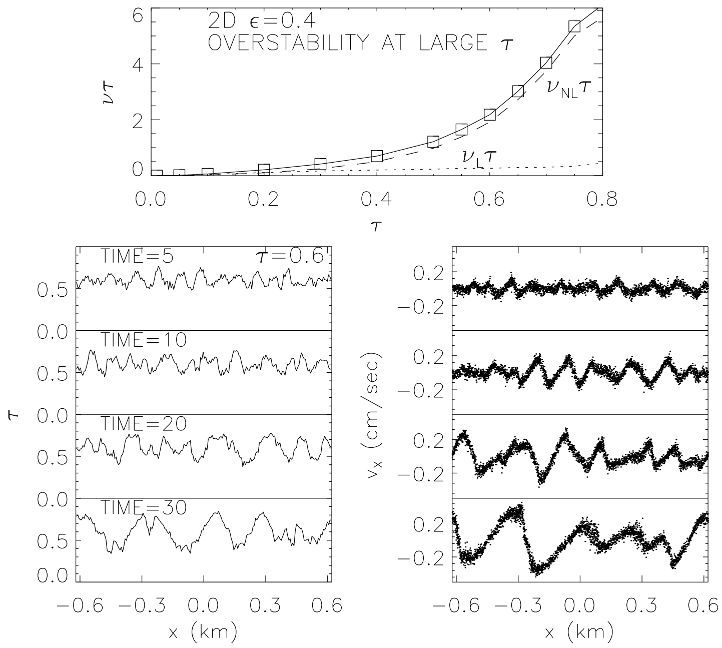

Fig. 10. Overstability in 2D simulation with $e_n = 0.4$. Two lower frames display evolution in a simulation with $\tau = 0.6$ ($L_x = 1240$ m, $L_y = 62$ m, $N = 15\ 000$)

For the same reason, ω_c increases in a very non-linear fashion as τ approaches the 2D close packing limit $\tau_{max} = \pi/\sqrt{12} \approx 0.91$. Due to the temperature dependency of ω_c, even a constant e_n close to unity can be balanced for a fixed τ, by increasing ω_c via $\sqrt{T}$. For small τ and e_n close to unity, $\nu \propto \tau^{-2}$, and the system fulfills the condition of viscous instability. Direct verification of this low-τ 2D instability requires much smaller N than the large-τ 3D instability, while it still represents the same physical mechanism. On the other hand, for large τ the strong non-linear growth of ω_c implies similar growth in ν_{NL}, so that β can become very large, implying tendency for overstability. Both types of behaviour are confirmed by direct 2D-simulations (see Figs. 9 and 10.)

In the example of Fig. 10, $\beta \approx 2.5$ for $\tau = 0.6$, exceeding the theoretical critical $\beta_{cr} \approx 0.11$ by a wide margin. Two-dimensional simulations with smaller τ, corresponding to smaller β, indicate that overstability is not obtained once β falls below ≈ 1.2. This limit is considerably larger than the theoretical β_{cr} found in [27]. The discrepancy is not due to special characteristics of 2D simulations: non-gravitating 3D near monolayer simulations ($\beta \approx 1$) show no signs of overstability, whereas corresponding simulations with vertical gravity ($\beta \approx 1.3$) are unstable. These, still preliminary results indicate that the existing stability analyses overestimate the tendency for overstability. One possible indication might be that the bulk viscosity, ξ, of a collisional ring may in fact exceed the kinematic shear viscosity: according to formulas in [27], the theoretical β_{cr} would rise to the level implied by direct simulations if $\xi/\nu > 4$. However, even then the expected theoretical growth times would be shorter than found in simulations, suggesting that some other factor might be missing from the stability analysis. Studies in this direction are in progress, together with Dr. Frank Spahn's group in Potsdam.

6 Summary

The collisional and gravitational dynamics of dense planetary rings have been reviewed through simulation examples. In principle, numerical simulations, combined with theoretical considerations, yield a fairly complete picture of the dependency of the local steady-state properties on the optical thickness, elastic properties, and size distribution. The major uncertainty, concerning the actual local properties of rings is due to uncertainty in elastic properties. Laboratory measurements indicate that particles' elasticity is very sensitive to their surface properties, which leads to a large range of possible physical situations, characterized by different kinetic temperature, and consequently by different vertical thickness and filling factor.

A possible diagnostic tool for accessing local properties is provided by self-gravity, whose importance depends crucially on the velocity dispersion via Toomre's Q_T-parameter. For example, application of Bridges et al. elasticity measurements leads to the formation of trailing particle wakes in simulations. On the other hand, less dissipative models suppress wakes. There is indirect evidence for the presence of such local particle chains, provided by the observed azimuthal asymmetry of Saturn's A-ring. On low elevation images the brightness of the A-ring depends on a bisymmetric manner on ring longitude with respect to observing direction (see e.g. [7]). For example, there is a definite minimum at longitude of 246^o, which can be accounted for by the presence of numerous small unresolved particle chains trailing on the average about 24^o with respect to tangential direction. Detailed photometric modelling of simulation data (Salo et al., in preparation) and comparison with the observed brightness asymmetry can in principle constrain both the elasticity and the internal density of particles. Preliminary results seem to support near monolayer models with $\rho \sim 0.5$ g/cm^3.

The mechanisms related to irregular radial structures in dense rings are still not completely understood. The originally proposed explanation in terms of viscous instability seems now outruled. A more promising candidate is the viscous overstability ([27], [28]), taking place when viscosity increases with density. Simulation examples of both these types of unstable behavior were given, utilizing 2-dimensional simulations. However, comparison of theoretically predicted range of overstability with simulations indicate that current theoretical models still need significant revisions: according to simulations the condition for overstability is much more stringent than predicted. Nevertheless, overstability is still obtained in 3D gravitating simulations, supporting this explanation for the B-ring structure.

In comparison to other types of granular systems dense planetary rings have quite special characteristics. Basically this is due to the presence of volume-forces depending on the planetocentric distance. This establishes a linear shear profile, and provides a steady energy source balancing the collisional dissipation. Also, the proportionality of vertical thickness to velocity dispersion (due to collisional energy partitioning) leads to impact frequency which depends essentially only on the optical thickness.

References

1. Araki, S., Tremaine, S. (1986) The dynamics of dense particle disks. Icarus **65** 83–109
2. Brahic, A. (1977) Systems of colliding bodies in a gravitational field. Astron. Astropys. **54**, 895–907
3. Bridges, F. G., Hatzes, A., Lin, D. N. C. (1984) Structure, stability and evolution of Saturn's rings. Nature **309**, 333–335
4. Brilliantov, N. V., Spahn, F. et al. (1996) Model for collisions in granular gases. Phys. Rev. E **53**, 5382–5392
5. Cuzzi, J. N., Durisen, R. H. et al. (1979) The vertical structure and thickness of Saturn's rings. Icarus **38**, 54–68
6. Dilley, J. P. (1993) Energy loss in collisions of icy spheres: Loss mechanism and size-mass dependence. Icarus **105**, 225–234
7. Dones, L., Cuzzi, J. N., Showalter, R. M. (1993) Voyager photometry of Saturn's A ring. Icarus **105**, 184–215
8. Goldreich, P., Tremaine, S. (1978) The velocity dispersion in Saturn's rings. Icarus **34**, 227–239
9. Goldreich, P., Tremaine, S. (1982) The dynamics of planetary rings. Ann. Rev. Astron. Astrophys. **20**, 249–284
10. Hatzes, A. P., F. G. Bridges, D. N. C. Lin (1988) Collisional properties of ice spheres at low impact velocities. Mon. Not. R. astr. Soc. **231**, 1091–1115
11. Hämeen-Anttila, K. A. (1978) An improved and generalized theory for the collisional evolution of Keplerian systems. Earth, Moon, and Planets **31**, 271–299
12. Hämeen-Anttila, K. A., Lukkari, J. (1980) Numerical simulations of collisions in Keplerian systems. Astrophys. Space Sci. **71**, 475–497
13. Hämeen-Anttila, K. A., Salo, H. (1993) Generalized theory of impacts in particulate systems. Earth, Moon, and Planets **62**, 47–84
14. Julian, W. H., Toomre, A. (1966) Non-axisymmetric responses of differentially rotating disks of stars. Astrophys. J. **146**, 810–827
15. Lin, D. N. C., Bodenheimer, P. (1981) On the stability of Saturn's rings. Astrophys. J. **248**, L83–L86
16. Lukkari, J. 1982. Collisional amplification of density fluctuations in planetary rings. Nature, **292**, 433–435
17. Lukkari, J, Salo, H. (1984) Numerical Simulations of Collisions in Self-Gravitating Systems. Earth, Moon, and Planets **31**, 1–13

18. Marouf, E. A., Tyler, G., L. et al. (1983) Particle size distribution in Saturn's rings from Voyager I radio occultation Icarus **54**, 189–211
19. Ohtsuki, K. (1993) Capture probability of colliding planetesimals: dynamical constraints on accretion of planets, satellites, and ring particles. Icarus **106**, 228–246
20. Richardson, D. C. (1993) A new tree code method for simulation of planetesimal dynamics. Mon. Not. R. astr. Soc. **264**, 396–414
21. Salo, H. (1987a) Collisional Evolution of Rotating, Non-Identical Particles. Earth, Moon, and Planets **38**, 149–181
22. Salo, H. (1987b) Numerical Simulations of Collisions between Rotating Particles. Icarus **70**, 37–51
23. Salo, H. (1991) Numerical simulations of dense collisional systems. Icarus **90**, 254–270. See also Erratum, Icarus **92**, 367–368
24. Salo, H. (1992a) Numerical simulations of dense collisional systems II: Extended distribution of particle sizes. Icarus **96**, 85–106
25. Salo, H. (1992b) Gravitational wakes in Saturn's rings. Nature **359**, 619–621
26. Salo, H. (1995) The dynamics of dense planetary rings III: Self-gravitating identical particles. Icarus **117**, 287–312
27. Schmit, U, Tscharnuter, W. M. (1995) A fluid dynamical treatment of the common action of self-gravitation, collisions, and rotation in Saturn's B-ring. Icarus **115**, 304–319
28. Schmit, U, Tscharnuter, W. M. (1999) On the formation of the fine-scale structure in Saturn's B-ring. Icarus **138**, 173–187
29. Spahn, F., Hertzsch, J.-M., Brilliantov, N. V. (1995) The role of particle collisions for the dynamics in planetary rings. Chaos, Solitons and Fractals **5**, 1945–1946
30. Stewart, G. R., Lin, D. N. C., Bodenheimer, P. (1984) Collision induced transport properties in planetary rings. In Planetary Rings (Eds. R. Greenberg, A. Brahic) pp. 447–512. Univ. of Arizona Press, Tucson
31. Supulver, K. D., Bridges, F., Lin, D. N. C. (1995). The coefficient of restitution of ice particles in glancing collisions: experimental results for unfrosted surfaces. Icarus **113**, 188–199
32. Toomre, A. (1964) On the gravitational stability of a disk of stars. Astrophys. J. **139**, 1217–1238
33. Toomre, A. (1990) Gas-hungry Sc spirals. In Dynamics and interactions of Galaxies (Ed. R. Wielen), pp. 292–303. Springer, Berlin
34. Trulsen, J. (1972) Numerical simulation of jet streams I: The three-dimensional case. Astrophys. Space Sci. **17**, 241–262
35. Weidenschilling, S., J., Chapman, C. R., et al. (1984) Ring particles: Collisional interactions and physical nature. In Planetary Rings (Eds. R. Greenberg, A. Brahic) pp. 367–415. Univ. of Arizona Press, Tucson
36. Ward, W. (1981) On the radial structure of Saturn's rings. Geophys. Res. Lett. **8**, 641–643
37. Wisdom, J., Tremaine, S. (1988) Local simulations of planetary rings. Astron. J. **95**, 925–940